• Supplementary File •

# Efficient charge transfer in $WS_2/W_xMo_{1-x}S_2$ heterostructure empowered by of energy level hybridization

Xuhong AN[1†], Yehui ZHANG[1†], Yuanfang YU[1], Weiwei ZHAO[1], Yutian YANG[1],
Xianghong NIU[3], Xuan LUO[2], Junpeng LU[1*], Jinlan WANG[1*] & Zhenhua NI[1*]

[1]*School of Physics and Key Laboratory of MESMS of the Ministry of Education,
Southeast University, Nanjing, 211189, China;*
[2]*Key Laboratory of Materials Physics, Institute of Solid State Physics,
Chinese Academy of Sciences, Hefei, 230031, China;*
[3]*New Energy Technology Engineering Laboratory of Jiangsu Province and School of Science,
Nanjing University of Posts and Telecommunications, Nanjing 210023, China*

*Theoretical calculation.* Time-dependent *ab initio* nonadiabatic molecular dynamics was performed to analyze the dependence of CTT on BO and hybridization strength in the $WS_2/W_xMo_{1-x}S_2$ heterostructure. Figures S1(a) and (b) show the variations of band structures of $WS_2/W_xMo_{1-x}S_2$ heterostructures at $x = 1$ and $x = 0$, respectively. According to the band structure characteristics, the valence and conduction bands are described by different colors. Bands mainly contributed by $W_xMo_{1-x}S_2$ are marked as blue, and bands mainly contributed by $WS_2$ are marked as red. The valence band maximum is derived from the joint contribution of $W_xMo_{1-x}S_2$ and $WS_2$, whereas the conduction band minimum (CBM) is dominated by $W_xMo_{1-x}S_2$. The insets in Figure S1(a) and (b) are the calculation models. For $x = 0$, Level 1/2 are completely degenerated at $\Gamma$ point. The energy difference between 1 and 3 reached a maximum value of 357 meV. At this point, BO dominated the CTR. With an increase in $x$, Level 1/2 splits into two due to the different energy of d orbitals between Mo and W atoms. Because the energy of the d orbitals of W (5d) is higher than Mo (4d), Level 1 arises from the interaction between the $d_z^2$ orbitals of Mo and the $p_x$ and $p_y$ orbitals of S atoms. In addition, Level 2 arises from the interaction between the $d_z^2$ orbital of W and the $p_x$ and $p_y$ orbitals of S atoms. With an increase in $x$, Level 3 (red band) slightly shifts to lower energy, whereas Level 1/2 shifts to higher energy. Therefore, for $WS_2/WS_2$, they are completely degenerated.
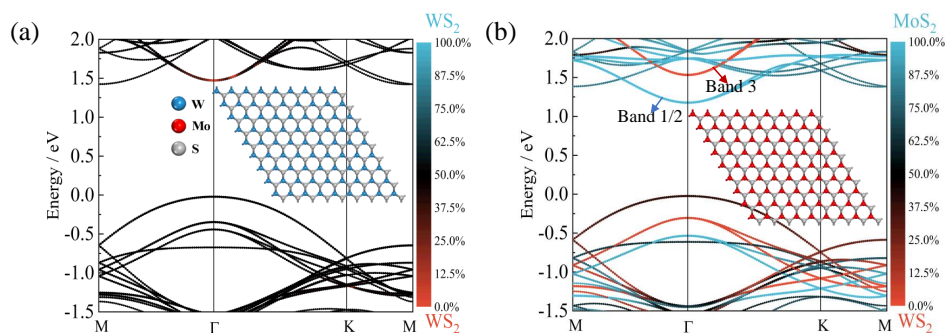


**Figure S1** Band structures of (a) $WS_2/WS_2$ ($x = 1$) and (b) $WS_2/MoS_2$ ($x = 0$); the insets are the top views of calculation models.

*Experimental section.* The $W_xMo_{1-x}S_2$ monolayer was directly grown on $SiO_2/Si$ (300 nm oxide layer) substrate via the chemical vapor deposition method; a schematic is shown in Figure S2(a). The

---

* Corresponding author (email: phyljp@seu.edu.cn, jlwang@seu.edu.cn, zhni@seu.edu.cn)
† Xuhong AN and Yehui ZHANG have the same contribution to this work.

optical image of $W_xMo_{1-x}S_2$ shown in the inset of Figure S2(d) depicts the regular triangle shape of the monolayer. Figure S2(c) shows the atomic force microscopy (AFM) image and height profile of the sample. The thickness of $\sim$0.8 nm indicates that the as-grown sample is a monolayer.[1] Raman spectra of $W_xMo_{1-x}S_2$ alloy are shown in Figure S2(b). WS$_2$-like $A_{1g}$ at 416.2 cm$^{-1}$ and MoS$_2$-like $A_{1g}$ at 394.6 cm$^{-1}$ originates from the out-of-plane vibrations of S atoms. WS$_2$-like $E^1_{2g}$ at 350.9 cm$^{-1}$ and MoS$_2$-like $E^1_{2g}$ at 373.7 cm$^{-1}$ originates from the in-plane vibrations of W/Mo and S atoms. Compared with bare MoS$_2$/WS$_2$, the stiffening/softening of the $A_{1g}$ mode of $W_xMo_{1-x}S_2$ is attributable to the larger bond energy in W-S than that in Mo-S.[2] The softening of the MoS$_2$-like $E^12g$ and slight shift of WS$_2$-like $E^1_{2g}$ in the alloy could be contributed to the large atomic weight of W.[3,4] These results confirm the formation of a ternary $W_xMo_{1-x}S_2$ alloy. As revealed by the photoluminescence (PL) mapping image [upper left corner inset of Figure S2(d)], the variation of the color from bright to dark corresponds to the reduction of PL intensity from the edge to center. The corresponding PL spectra are shown in Figure S3(a). Meanwhile, no sudden break or jump in PL position line scanning occurs along the direction of blue arrow in the insert of Figure S2(d). The specific W composition ($x$) can be determined by[1,5]

$$E_{PL,W_xMo_{1-x}S_2} = xE_{WS_2} + (1-x)E_{MoS_2} + bx(1-x) \tag{1}$$

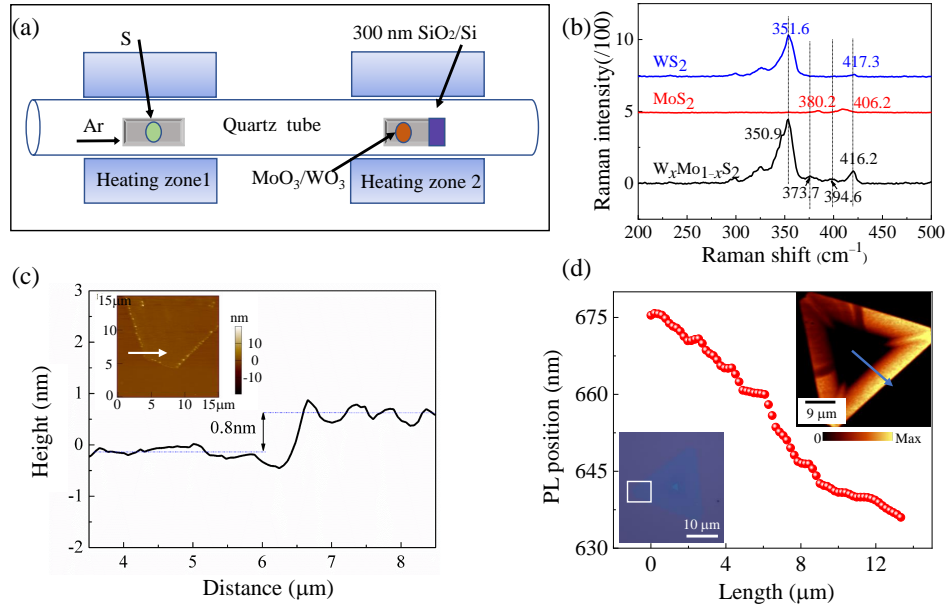In our system, the W composition $x$ of Sample 1 varies from 0.45 to 0.95 [Figure S3(b)].



**Figure S2** The grown and characterization of $W_xMo_{1-x}S_2$. (a) Schematic of the set-up employed for the growth of ternary alloy monolayers. (b) Raman spectra of WS$_2$, MoS$_2$, $W_xMo_{1-x}S_2$. (c) AFM height profile along red line in the inset. Insert is AFM image. (d) PL peak positions along blue arrow from the edge to center. The left inset shows PL mapping of monolayer $W_xMo_{1-x}S_2$ alloy and right inset is the optical image.

Figure S4 shows the Raman mapping images [Figures S4(a-d)] of Sample 1 and PL mapping images of Sample 2 [Figures S4(e, f)]. Raman signal enhancement is observed at 352 cm$^{-1}$ and 420 cm$^{-1}$ in heterostructure, whereas quenching is observed at 377 and 396 cm$^{-1}$. PL intensities of WS$_2$ stacking in the region of $W_xMo_{1-x}S_2$ with $0 < x < 0.7$ are significantly reduced, but it is not completely quenched. The PL intensities of $W_xMo_{1-x}S_2$ are also reduced as shown in [Figures S4(g, h)]. The PL peak of $W_xMo_{1-x}S_2$ is broadened and slightly shifted, which can be explained by the lifetime effect resulting from the decay of excitons initially created in the $W_xMo_{1-x}S_2$ layer through CT processes.[6]

Figures S5(a) and (b) depict the PL spectra of $W_xMo_{1-x}S_2$ and WS$_2$/$W_xMo_{1-x}S_2$ heterostructures ($x = 0.8$) at a low temperature of 10 K. For bare $W_xMo_{1-x}S_2$ ($x = 0.8$), three peaks at 1.964, 1.933, and 1.889 eV are observed, and they are assigned to exciton, trion, and defect-related recombination, respectively. The energy separation between two peaks at 1.964 and 1.933 eV is $\sim$31 meV, which agrees with the trion binding energy. The reported trion binding energy of WS$_2$ and MoS$_2$ monolayers are 42 meV and 39 meV, respectively.[7] For the WS$_2$/$W_xMo_{1-x}S_2$ heterostructure ($x = 0.8$), the PL of WS$_2$
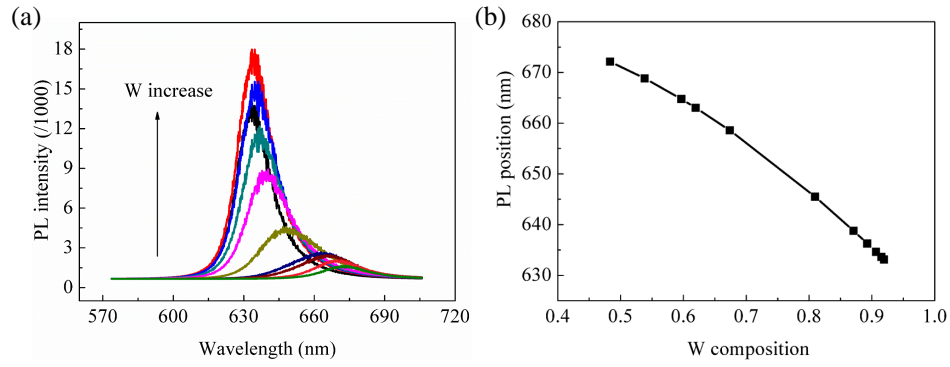
**Figure S3** PL spectra and composition. (a) The variations of PL spectra from the center to edge. (b) PL position as a function of W composition.
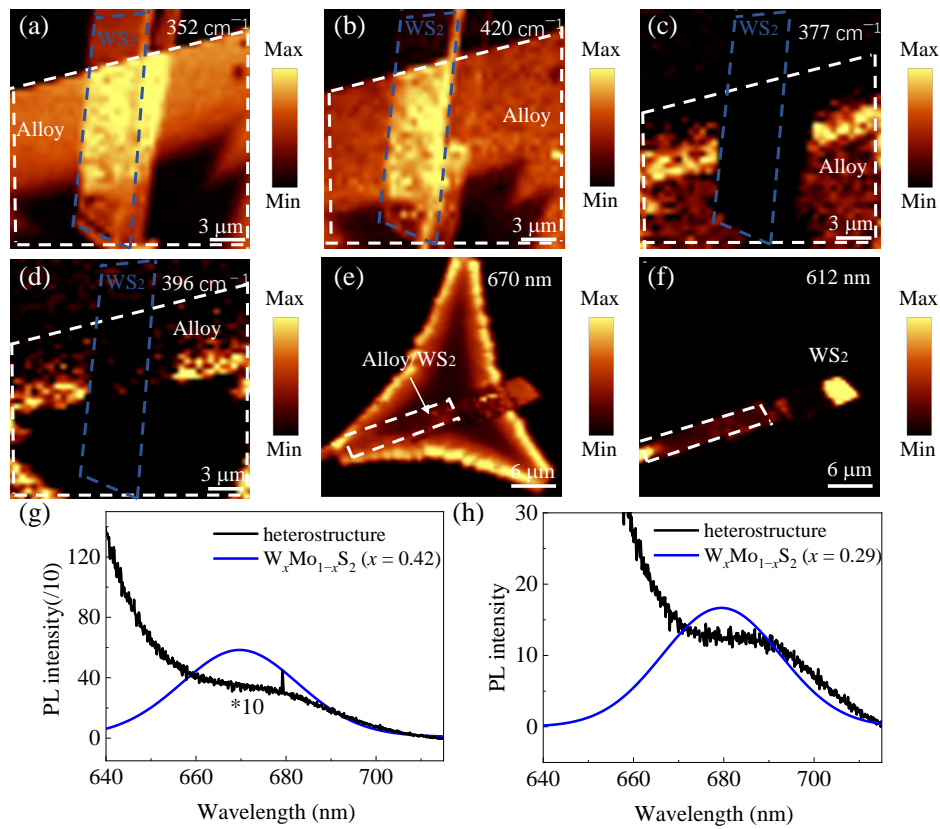


**Figure S4** Raman and PL characterization. (a-c) Raman mapping images of $WS_2/W_xMo_{1-x}S_2$ heterostructures (Sample 1) at 352, 420, 377, and 396 cm$^{-1}$, respectively; scale bar = 3 $\mu$m. (e) and (f) PL mapping images of Sample 2 centered at 670 and 620 nm, respectively. Scale bar = 6 $\mu$m. (g) and (h) PL spectra of heterostructure and bare $W_xMo_{1-x}S_2$ for $x = 0.42$ and 0.29, respectively.

is completely quenched, whereas the PL of $W_xMo_{1-x}S_2$ is significantly reduced. The exciton and trion peaks of $W_xMo_{1-x}S_2$ shift to lower energy at 1.962 eV and 1.928 eV, respectively.
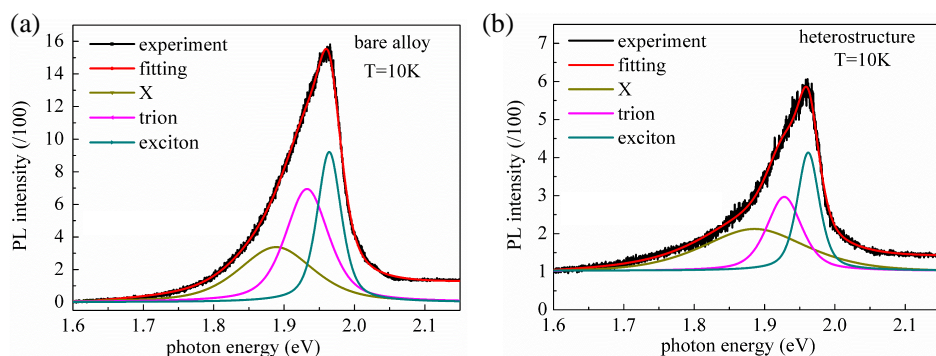


**Figure S5** PL characterization at 10 K. PL spectra of (a) bare alloy and (b) heterostructure with $x = 0.8$ at 10 K.

The PL quenching degree of $WS_2$ depends strongly on the W composition ($x$). It is completely quenched at $0.7 < W < 1$, and the quenched degree of $WS_2$ generally decreases with $x$. To further demonstrate the dependence of PL quenching on $x$, comparison experiments were performed on $WS_2/WS_2$ and $WS_2/MoS_2$ (Figure S6). The optical image of $WS_2/WS_2$ homostructure is shown in Figure S6(a), and the region of homostructure region is highlighted by the white dotted line. The PL intensity of $WS_2$ is significantly reduced by about six times, as revealed by the PL mapping image [Figure S6(b)] and PL spectrum [Figure S6(c)]. More $WS_2/WS_2$ samples were investigated. The degree of PL quenching differs due to the difference in their stacking order. This phenomenon has been reported for $MoS_2/MoS_2$.[8] The optical image of $WS_2/MoS_2$ heterostructure is shown in Figure S6(d). The PL of $WS_2$ is significantly reduced by about 21 times, as revealed by the PL mapping image [Figure S6(e)] and PL spectrum [Figure S6(f)].
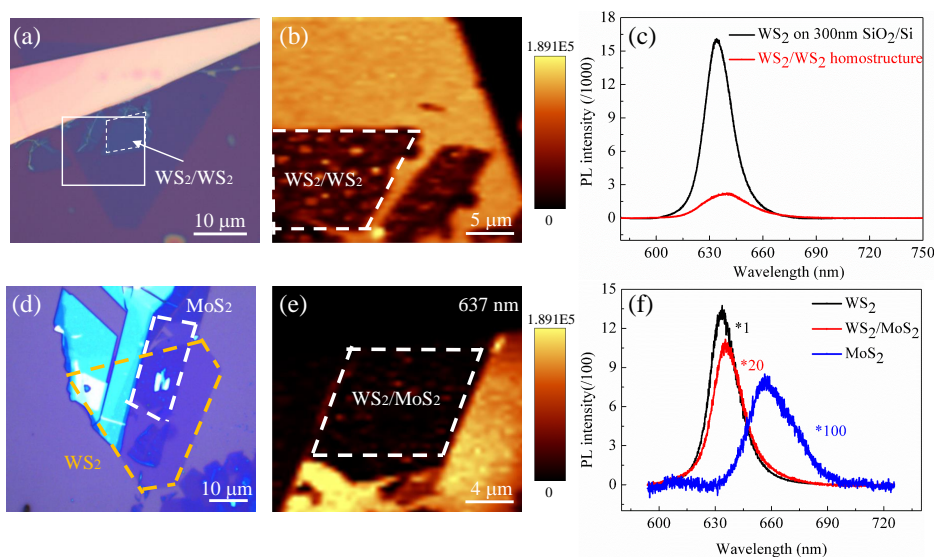


**Figure S6** PL characterization of $WS_2/WS_2$ homostructure and $WS_2/MoS_2$ heterostructure. (a) Optical image of $WS_2/WS_2$ homostructure. (b) PL mapping image of $WS_2/WS_2$ homostructure extracted from white solid box in (a). (c) PL spectra of bare $WS_2$ and $WS_2/WS_2$ homostructure. (d) Optical image of $WS_2/MoS_2$ heterostructure. (e) PL mapping image of $WS_2/MoS_2$, heterostructure. (f) PL spectra of $WS_2$, $WS_2/MoS_2$ and $MoS_2$.

**References**

1   Chen Y, Xi J, Dumcenco D O, et al. Tunable band gap photoluminescence from atomically thin transition-metal dichalcogenide alloys. ACS nano, 2013, 7: 4610-4616

2   Zhang W, Li X, Jiang T, et al. CVD synthesis of $Mo_{1-x}W_xS_2$ and $MoS_{2(1-x)}Se_{2x}$ alloy monolayers aimed at tuning the bandgap of molybdenum disulfide. Nanoscale, 2015, 7: 13554-13560

3   Mao N, Chen Y, Liu D, et al. Solvatochromic effect on the photoluminescence of $MoS_2$ monolayers. Small, 2013, 9: 1312-1315

4  Liu X, Wu J, Yu W, et al. Monolayer $W_x Mo_{1-x} S_2$ grown by atmospheric pressure chemical vapor deposition: bandgap engineering and field effect transistors. Advanced Functional Materials, 2017, 27: 1606469

5  Zheng S, Sun L, Yin T, et al. Monolayers of $W_x Mo_{1-x} S_2$ alloy heterostructure with in-plane composition variations. Applied Physics Letters, 2015, 106: 063113

6  Rigosi A F, Hill H M, Li Y, et al. Probing interlayer interactions in transition metal dichalcogenide heterostructures by optical spectroscopy: $MoS_2/WS_2$ and $MoSe_2/WSe_2$. Nano Letters, 2015, 15: 5033-5038

7  Jadczak J, Kutrowska-Girzycka J, Kapuscinski P, et al. Probing of free and localized excitons and trions in atomically thin $WSe_2$, $WS_2$, $MoSe_2$ and $MoS_2$ in photoluminescence and reflectivity experiments. Nanotechnology, 2017, 28: 395702

8  Ji Z, Hong H, Zhang J, et al. Robust stacking-independent ultrafast charge transfer in $MoS_2/WS_2$ bilayers. ACS nano, 2017, 11: 12020-12026